PCCP

PAPER

View Article Online
View Journal | View Issue

Cite this: *Phys. Chem. Chem. Phys.*, 2017, **19**, 15933

Investigation of interfacial thermal transport across graphene and an organic semiconductor using molecular dynamics simulations†

Xinyu Wang,[a] Jingchao Zhang,[b] Yue Chen*[a] and Paddy K. L. Chan*[a]

Received 27th March 2017,
Accepted 19th May 2017

DOI: 10.1039/c7cp01958k

rsc.li/pccp

The interfacial thermal transport across graphene and an organic semiconductor, dinaphtho[2,3-*b*:2′,3′-*f*]-thieno[3,2-*b*]thiophene (DNTT), is investigated using molecular dynamics simulations. The average thermal boundary resistance (TBR) of graphene and DNTT is 4.88 ± 0.12 × 10^{-8} m^2 K W^{-1} at 300 K. We find that TBR of a graphene–DNTT heterostructure possesses as high as 83.4% reduction after the hydrogenation of graphene. Moreover, as the graphene vacancy increases from 0% to 6%, the TBR drops up to 39.6%. The reduction of TBR is mainly attributed to the coupling enhancement of graphene and DNTT phonons as evaluated from the phonon density of states. On the other hand, TBR keeps a constant value while the vacancy in the DNTT layer increases. The TBR would decrease when the temperature and coupling strength increase. These findings provide a useful guideline for the thermal management of the graphene-based organic electronic devices, especially the large area transistor arrays or sensors.

1. Introduction

The unique electrical and thermal properties of graphene open up a new research area in flexible electronics for both active layers and electrodes.[1–6] For example, graphene-based transistors not only operate at gigahertz frequencies as high as 100 GHz,[7,8] but also possess a high carrier mobility[2] of around 10 000 cm^2 V^{-1} s^{-1}, which shows their tremendous potential in nanoscale electronic devices. The superior in-plane thermal conductivity of graphene also allows effective heat dissipation for the electronic devices. Theoretical and experimental investigations have demonstrated that in-plane thermal conductivity of graphene can reach 2000–6000 W m^{-1} K^{-1} measured or calculated by using confocal micro-Raman spectroscopy,[6] the suspended micro-bridge method,[9] molecular dynamics simulations[9] and first-principles calculations.[10] These physical properties of graphene have been further optimized and investigated under different structures including nanoribbons,[11] stacked bilayers,[12] or multilayers,[2] or chemical treatment.[13,14]

Other than the pure graphene-based investigation, its interaction with other semiconductors primarily organic semiconductors has also become a popular research topic in the last decade. Organic active layers with graphene as the conductive electrode have been further broadening the horizons of this new class of flexible electronics.[15–17] One important aspect of such a graphene–organic device is the energy band alignment. Park *et al.* reported that the work function of graphene could be optimized by functionalizing the substrate with self-assembled monolayers (SAMs) and reducing the charge injection barrier in organic field effect transistors (OFETs).[15] On the other hand, the carrier mobility in the polymer OFETs could be increased 20 times by embedding graphene flakes into the polymer active layer.[18] The performance of these contacting electrodes or active layers strongly depends on the interface quality between the organic semiconductor and graphene. While the current density and functionality of these graphene–organic hybrid devices are increasing, the generation of wasted heat in these devices would become critical to the overall performance. As we know that the molecular alignment and the surface morphology of the organic semiconductors are sensitive to the thermal environment of devices,[19–21] inferior heat transportation would directly affect the device lifetime. Given that graphene has the excellent thermal conductivity, the mechanism of heat propagation through this graphene–organic interface would be a critical parameter in governing the heat dissipation in these devices. Furthermore, different from the graphene–inorganic interfaces which have been simulated[22–25] or measured,[26] investigation about an interfacial thermal transport of graphene–organic semiconductors is still very limited.

Molecular dynamics (MD) simulations have widely been applied to investigate the thermal properties of the graphene-based

[a] *Department of Mechanical Engineering, The University of Hong Kong, Hong Kong. E-mail: pklc@hku.hk, yuechen@hku.hk*
[b] *Holland Computing Center, University of Nebraska-Lincoln, Lincoln, NE 68588, USA*

† Electronic supplementary information (ESI) available. See DOI: 10.1039/c7cp01958k

structures, which can not only overcome the measurement difficulties of experiments but also provide the atomic-level insights into thermal transport.[3,27] Other than the intrinsic thermal properties of graphene with defects,[28–30] doping[31,32] or chemical functionalization[33–36] predicted by MD, the in-plane and out-of-plane interfacial thermal transports between graphene and other materials have also been calculated by MD simulations,[23,25,26,37–42] which provide the useful thermal knowledge for the application of graphene. In this work, we focus on investigating the interfacial thermal transport of graphene and an air-stable small molecule organic semiconductor, dinaphtho-[2,3-*b*:2′,3′-*f*]thieno[3,2-*b*]thiophene (DNTT), using classical MD simulations. OFETs with DNTT active layers have been showing a promising carrier mobility of up to 9.9 $cm^2 V^{-1} s^{-1}$ in single crystal structures[43] and are thermally stable up to 100 °C. By using the 3-ω method, we measured the thermal conductivity (k) of DNTT (k = 0.45 ± 0.06 W $m^{-1} K^{-1}$) and suggested an approach to modulate the k values by embedding silver nanoparticles.[44] Very recently, we utilized molecular dynamics to simulate the thermal conductivity of DNTT and obtained the bulk thermal conductivities of DNTT along the a^*, b^* and c^* directions as 0.73, 0.33 and 0.95 W $m^{-1} K^{-1}$.[45] Meanwhile, the thermal boundary resistances across different orientation interfaces were calculated as 7.00 ± 0.26, 6.15 ± 0.13 and 3.20 ± 0.09 × 10^{-9} m^2 K W^{-1} for the a^*–b^*, a^*–c^* and b^*–c^* interfaces, respectively. Here we apply a transient heating method in the MD simulations to mimic the experimental pump–probe technique and evaluate the thermal boundary resistance (TBR) between graphene and DNTT. We firstly study the effects of the graphene dimension and the DNTT thickness on the TBR values. Secondly, we investigate the effects of the graphene hydrogenation and vacancy concentration. We further extend the work by simulating the TBR at different temperatures and interfacial coupling strengths between graphene and DNTT. The phonon density of states (DOS) of graphene and DNTT are also calculated respectively to analyze the TBR results.

2. Theory and modeling

The MD simulations are performed using the Large-scale Atomic/Molecular Massively Parallel Simulator (LAMMPS) package.[46] The second-generation reactive empirical bond order (REBO) potential has been reported to model C–C interactions[47] in graphene and accurately predict the thermal properties of graphene.[5,22,23,48,49] Meanwhile, various works have demonstrated that the general AMBER force field (GAFF)[50] is able to account for the intermolecular and intramolecular interactions of small molecule organic semiconductors, such as pentacene,[51,52] DNTT,[45] and 2,7-dioctyl[1]benzothieno[3,2-*b*][1]-benzothiophene (C8-BTBT).[53] Therefore, we employ the REBO potential to describe the C–C interactions in graphene and adopt GAFF to describe the bond, angle, dihedral, van der Waals and electrostatic interactions in the DNTT molecules. In addition, Lennard-Jones (L-J) potential is employed to describe the van der Waals interactions between graphene and DNTT as below:

$$E_{LJ} = 4\chi\varepsilon\left[\left(\frac{\sigma}{r}\right)^{12} - \left(\frac{\sigma}{r}\right)^{6}\right] \quad (1)$$

where, r is the distance between atoms; ε is the depth of the potential well; σ is the zero energy separation distance; and χ is the coupling strength factor to adjust the interaction strength between graphene and DNTT. The L-J potential parameters are calculated from the universal force field (UFF).[54] The details of the GAFF and UFF parameters used in the simulations are summarized in the ESI.† The development of the DNTT molecules in the system is based on the DNTT structure reported by Yamamoto and Takimiya.[55] In the simulations, graphene is perpendicularly placed on the c direction of the DNTT crystals. The zigzag direction of graphene and the a direction of the DNTT lattice are along the x direction of the simulation box while the armchair direction of graphene and the b direction of the DNTT lattice are along the y direction of the simulation box.

To calculate the thermal boundary resistance between graphene and DNTT, a transient heating method,[22,25,49,56,57] which is

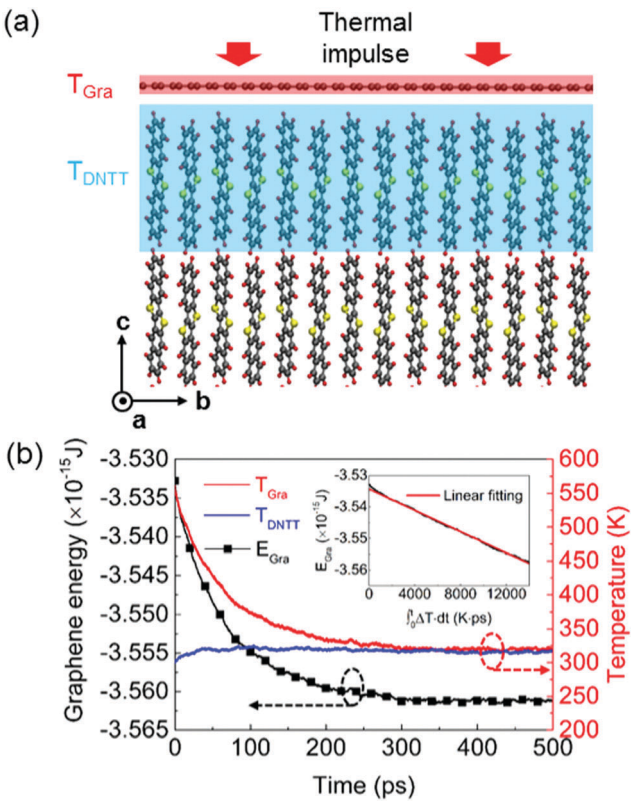

Fig. 1 (a) Schematic illustration of the graphene–DNTT heterostructure. A 50 fs thermal impulse is inputted on graphene. The temperature of graphene (red region), T_{Gra}, and temperature of DNTT monolayer close to the interface (blue region), T_{DNTT}, are recorded as a function of time. (b) The energy evolution of graphene during the 500 ps relaxation process (left y-axis) and the temperature evolution of graphene and single DNTT layers during the 500 ps relaxation process (right y-axis). The inset figure shows the linear fitting of energy with temperature difference integration based on eqn (3).

similar to the experimental pump–probe method, is applied in the simulations. As shown in Fig. 1(a), an ultrafast thermal impulse is imposed on graphene, and thus the energy and temperature of graphene will be increased rapidly. During the subsequent thermal relaxation process, the thermal energy will propagate from graphene to DNTT. Therefore, energy and temperature of graphene will drop gradually whereas the energy and temperature of DNTT go up as shown in Fig. 1(b). The interfacial thermal transport during thermal relaxation process will obey the following equation:

$$\frac{\partial E_{\mathrm{Gra}}}{\partial t} = A \cdot \frac{T_{\mathrm{Gra}} - T_{\mathrm{DNTT}}}{R} \tag{2}$$

where, E_{Gra} is the energy of graphene; T_{Gra} and T_{DNTT} are the temperatures of graphene and DNTT monolayers next to the interface; t is the time; A is the graphene area; and R is the TBR. We can integrate eqn (2) to obtain:

$$E_{\mathrm{Gra},t} - E_{\mathrm{Gra},0} = \frac{A}{R} \cdot \int_0^t (T_{\mathrm{Gra}} - T_{\mathrm{DNTT}})\mathrm{d}t \tag{3}$$

The inset of Fig. 1(b) shows the curve of E_{Gra} and $\int_0^t (T_{\mathrm{Gra}} - T_{\mathrm{DNTT}})\mathrm{d}t$, which demonstrates that their relation is close to linear. By linear fitting and knowing the graphene area, the TBR values can be evaluated from the slope of eqn (3).

In our MD simulations, the periodic boundary conditions along x and y directions and free boundary conditions along the z direction are used and the time step is chosen to be 0.5 fs. To develop and apply periodic boundary conditions along x and y directions, the lattice constant of graphene is modified, which induces a lattice modification of 0.602% along the x direction and −0.102% along the y direction for the structure of graphene. This modification has a negligible effect on the TBR values and will be discussed later. The graphene atoms are initially positioned at 3.4 Å on top of the DNTT molecules. In the beginning, the system is equilibrated in a canonical (*NVT*) ensemble for 0.5 ns at the specified temperature. Afterward, a microcanonical (*NVE*) ensemble is performed on the system for another 0.5 ns. When the system reaches the *NVE* equilibrium, an ultrafast thermal impulse (8×10^{12} W m^{-2}) is exerted on graphene. By monitoring the energy and temperature for the following 0.5 ns, the TBR can be extracted based on the fitting method discussed above. For each TBR value, more than three independent simulations with different initial conditions are performed. The TBR values are calculated by averaging each simulation with the error bar as the standard deviation. To verify the effect of the DNTT orientation, we build the structures of graphene placed on the a and b directions of the DNTT crystals. No obvious TBR variation can be observed at different DNTT orientations and the results are shown Fig. S1 in the ESI.† In the following parts, all the simulations are based on the structure of graphene placed on the c direction of DNTT.

To reveal the interfacial energy transport physics and interpret the TBR results of graphene and DNTT, the phonon DOS is calculated by taking the Fourier transform of the velocity autocorrelation function (VACF):[3,49,56]

$$P(\omega) = \frac{1}{\sqrt{2\pi}} \int_{-\infty}^{\infty} \mathrm{e}^{i\omega t} \frac{\langle \boldsymbol{v}(t) \cdot \boldsymbol{v}(0) \rangle}{\langle \boldsymbol{v}(0) \cdot \boldsymbol{v}(0) \rangle} \mathrm{d}t \tag{4}$$

where $P(\omega)$ denotes the phonon DOS at frequency ω, and $\boldsymbol{v}(t)$ and $\boldsymbol{v}(0)$ are atom velocity vectors at t time and zero time, respectively. According to the value of phonon DOS, we can analyze the energy transport mechanism of graphene and DNTT. Meanwhile, the overlapping of phonon DOS of graphene and DNTT is an indicator of the phonon transmission capacity across the interface between graphene and DNTT. To compare the phonon DOS in the same baseline, we firstly normalize the total phonon DOS areas of graphene and DNTT to 1, respectively. To quantify phonon transmission capacity, we adopt a phonon overlapping factor (arbitrary unit), which is defined as $\delta = \int H(\omega)\mathrm{d}\omega$,[58] where $H(\omega)$ represents the intersection height of normalized phonon DOS at frequency ω, to analyze the TBR results. The total intersection area of phonon DOS is proportional to the amount of energy transported across the interface.

3. Results and discussion

3.1 Effects of graphene dimension and DNTT thickness

As we know, due to the long phonon mean free path (MFP) of graphene, the in-plane thermal conductivity of graphene strongly depends on the dimension.[59] To investigate the effects of the graphene dimension and the DNTT thickness on the interfacial thermal transport between graphene and DNTT, we develop a simulation dimension with different graphene areas and DNTT thicknesses. In this part, the system is initially equilibrated at 300 K. The interface coupling strength factor (χ) is set as unity.

Five sizes of graphene ($x \times y$) are built as 2.475 × 7.662, 4.950 × 7.662, 9.899 × 7.662, 14.849 × 7.662, and 19.798 × 7.662 nm^2. The corresponding DNTT $x \times y$ ($a \times b$) dimension changes with the graphene dimension and the thickness of DNTT (c, along the z direction) is fixed at 8.096 nm. From the results shown in Fig. 2, it can be noticed that TBR values

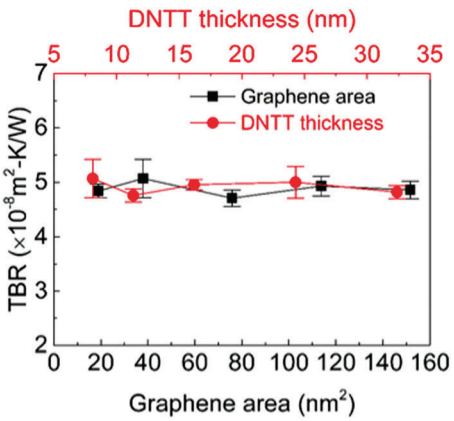

Fig. 2 TBR variation of graphene and DNTT at different graphene areas and DNTT thicknesses.

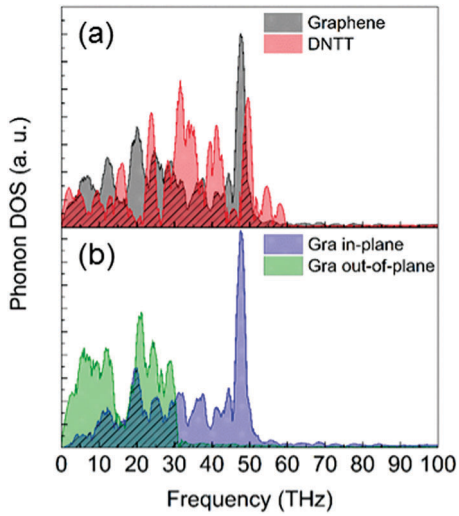

Fig. 3 (a) Phonon DOS of total graphene and DNTT. (b) Phonon DOS of in-plane and out-of-plane graphene. Slanted line areas denote overlap of phonon DOS. The phonon overlapping factor of graphene and DNTT is 0.598; and the phonon overlapping factor of in-plane and out-of-plane phonons in graphene is 0.443.

remain constant even when the graphene area has an 8-fold increase. We also investigate the dependence of TBR on the DNTT thickness (z direction) by fixing the graphene dimension (4.950×7.662 nm^2) and enlarging the thickness of the DNTT layers (8.096, 11.335, 16.193, 24.289, and 32.385 nm). Similar to the graphene areas, TBR values remain relatively constant for various thicknesses of DNTT. We can conclude that TBR of graphene–DNTT is irrelevant to the graphene dimension and the DNTT thickness. By averaging the TBR values at different dimensions, the TBR of graphene–DNTT is $4.88 \pm 0.12 \times 10^{-8}$ m^2 K W^{-1}, which is similar to TBR values of graphene–silicon,[22] graphene–paraffin wax[60] and graphene–octane.[61,62]

Fig. 3(a) shows the phonon DOS of graphene and DNTT. It can be observed that the major energy channel (overlapping region) of DNTT and graphene is located at the mediate frequency ranging from 20 THz to 52 THz. Even though more long-wavelength (low-frequency) phonons can participate in energy transport by increasing the graphene dimension and DNTT thickness, low-frequency phonons just make a small contribution to the interfacial thermal transport between graphene and DNTT. Therefore, we cannot observe the significant size dependence of TBR for the graphene–DNTT heterostructure.

To address the effects due to modifying the lattice constant of graphene in order to satisfy the periodic boundary condition in the model, we also repeat the simulations with a pristine graphene lattice constant equal to 2.46 Å and the results are shown in Fig. S2 in the ESI.† The DNTT simulation system in free boundary conditions along x and y directions and five kinds of graphene sizes are simulated as well. By comparing these two kinds of graphene structures, we find that it can be noticed that there is no significant variation for TBR values when the lattice of graphene is stretched 0.602% along the x direction while contracted 0.102% along the y direction. It can be concluded that this slight lattice modification of graphene cannot bring about the effect to the TBR. In the following sections, the lattice constant of graphene is modified and periodic boundary conditions are applied in the simulations.

3.2 Effects of graphene hydrogenation

One commonly adopted approach to functionalize graphene is using chemical processes such as hydrogenation,[13,14,35,39,63–65] fluorination,[66] and chemical function group treatment[36] to tune the electrical,[13,14] thermal,[35,64] mechanical[63] and magnetic[65] properties of graphene. To overcome the zero-bandgap nature of pristine graphene and achieve the desired electrical properties of graphene, hydrogen is widely used to functionalize graphene to control the energy band gap,[13] carrier mobility and the on/off ratio of the transistor,[13] and magnetic states,[14,67] where sp^2 C bonding hybridization in graphene changes into sp^3 hybridization. Accompanied by the hydrogenation-enhanced electrical properties, the generated thermal issues of the devices are unneglectable and they affect the performance and lifetime of these devices. As a result, it is essential to investigate the interfacial thermal transport between hydrogenated graphene (H-graphene) and the organic semiconductor in graphene-based organic electronic devices.

The hydrogenation process is shown in the schematic structure shown in Fig. 4 where hydrogen atoms are added to carbon atoms of graphene on both sides alternately, and the hydrogenated graphene sheet perpendicularly lies on the DNTT c direction. We define the hydrogen coverage ratio (α) as $\alpha = \frac{N_H}{N_{Gra}}$, where N_H is the atom number of hydrogen and N_{Gra} is the atom number of graphene. When α is equal to 100%, hydrogenated graphene is known as graphane.[68] In order to minimize the effects of the hydrogen distribution, the hydrogen atoms are added randomly to graphene. The in-plane dimension of graphene is 4.950×7.662 nm^2 ($x \times y$) and the DNTT thickness is chosen as 8.096 nm. The *NVT* equilibrium temperature is 300 K and χ is still maintained at 1. Fig. 4 shows the TBR variation of H-graphene and DNTT as a function of hydrogen coverage ranging from 0% to 100%. It can be noted that TBR will drop dramatically from $5.07 \pm 0.35 \times 10^{-8}$ m^2 K W^{-1} to $1.07 \pm 0.13 \times 10^{-8}$ m^2 K W^{-1}

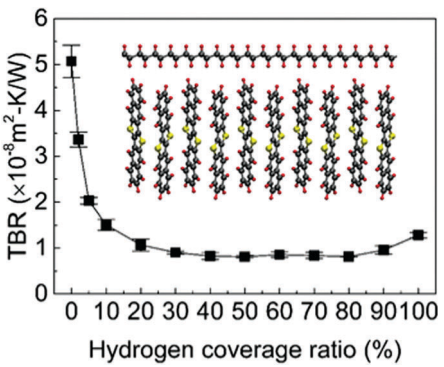

Fig. 4 TBR variation of graphene and DNTT at different hydrogen coverage ratios. The inset figure shows the illustration of the hydrogenated graphene–DNTT heterostructure.

when the hydrogen coverage ratio increases from 0% to 20%. When the hydrogen coverage ratio ranges from 30% to 80%, the TBR reaches a constant value, around 8.4×10^{-9} m^2 K W^{-1}, which is only around 16.6% of TBR of pristine graphene and DNTT. With a further increase of the hydrogen coverage ratio from 90% to 100%, the TBR shows a slight enhancement. This observation agrees with the previous studies that the thermal conductivity of hydrogenated graphene drops obviously from 0% to 20%, then levels off and finally increases.[34,35,64]

The underlying physical mechanism about the TBR reduction after hydrogenation is further explored by evaluating the phonon DOS of H-graphene, DNTT and hydrogen with 10%, 50% and 100% hydrogen coverage ratios as shown in Fig. 5. It can be observed that by comparing the phonon DOS of pristine graphene (Fig. 3) and H-graphene, the shape of in-plane, out-of-plane and total phonon DOS of graphene shows a remarkable deformation. Due to the light atom mass of hydrogen, the hydrogen atom vibrates at a high frequency as shown in Fig. 5(g–i). The hydrogen additionally broadens the total phonon DOS of graphene and brings about a high-frequency peak at approximately 87 THz (Fig. 5(a–c)). Meanwhile, the G-band peak (around 47.7 THz) of graphene DOS is weakened and shows a shift to a high frequency for hydrogen coverage ratios of 10% and 50%. Based on Fig. 3(a) and 5(a–c), we can calculate the phonon overlapping factor (δ) of graphene and DNTT as 0.598, 0.647, 0.653 and 0.580 for hydrogen coverage ratios of 0%, 10% and 50% and 100%, respectively. The phonon overlapping factor gives a direct explanation for the TBR variation trend, which firstly drops, then saturates and finally increases. In supported graphene, due to phonon scattering at supporting atoms, in-plane and out-of-plane phonons of graphene are coupled, and this coupling effect plays an important role in energy propagation.[39,69] Zhang *et al.* have found that the energy conversion between in-plane transverse (TA) and longitudinal (LA) phonons was much faster than that between in-plane (TA/LA) and out-of-plane (ZA) phonons.[5] Therefore, thermal resistance of the energy conversion in supported graphene majorly comes from the conversion between in-plane and out-of-plane phonons. Fig. 3(b) and 5(d–f) exhibit in-plane and out-of-plane phonon DOS of graphene. The adding of hydrogen atoms suppresses the G-band frequency of the in-plane phonon mode, broadens the out-of-plane phonon mode, and shifts the out-of-plane phonon mode to a high frequency. The calculated δ values of in-plane and out-of-plane phonons in graphene are 0.443, 0.579, 0.674 and 0.713 for hydrogen coverage ratios 0%, 10%, 50% and 100%, respectively. These results indicate that the hydrogen atoms generate more graphene phonon scattering centers, which will strengthen the energy conversion between in-plane and out-of-plane phonons in graphene. The improved energy conversion between in-plane and out-of-plane phonons is beneficial to heat transfer from the in-plane to out-of-plane phonons in graphene, which indirectly enhances the interfacial thermal conductance between graphene and the DNTT phonons. Moreover, the hydrogen atoms act as another participant to interact with atoms in DNTT molecules, which opens up a new channel to transport energy across the interface.

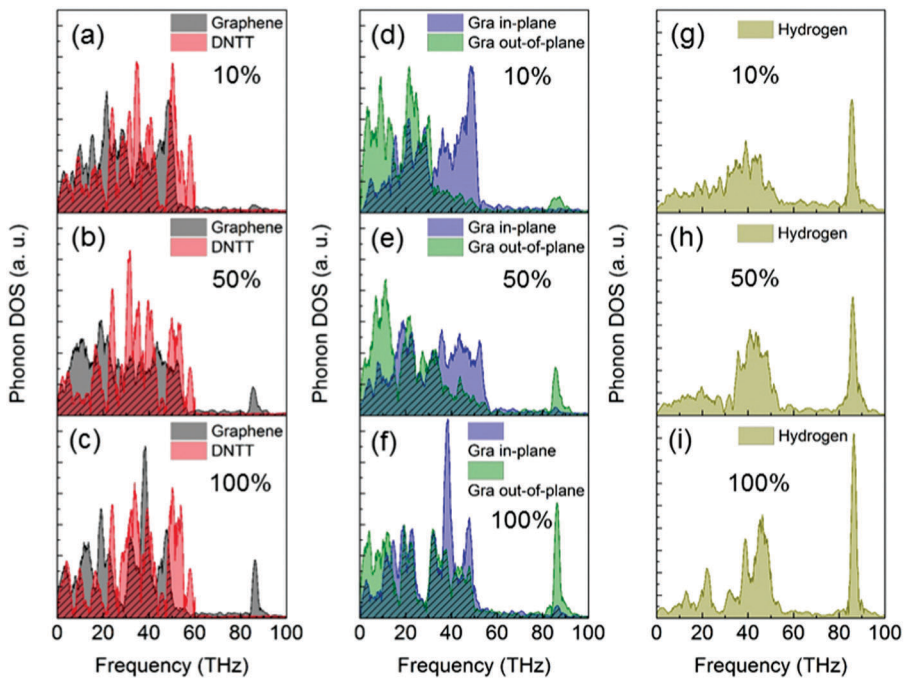

Fig. 5 (a–c) Phonon DOS of total graphene and DNTT at hydrogen coverage ratio of 10%, 50% and 100%. (d–f) Phonon DOS of in-plane and out-of-plane graphene at hydrogen coverage ratio of 10%, 50% and 100%. (g–i) Phonon DOS of hydrogen atoms at hydrogen coverage ratio of 10%, 50% and 100%. Slanted line areas denote overlap of phonon DOS. The phonon overlapping factors of graphene and DNTT are 0.647, 0.653 and 0.580 at hydrogen coverage ratio of 10%, 50% and 100%; and the phonon overlapping factors of in-plane and out-of-plane phonons in graphene are 0.579, 0.674 and 0.713 at hydrogen coverage ratio of 10%, 50% and 100%.

A slight increase of TBR with a hydrogen coverage ratio of 80–100% is attributed to the reduction of phonon overlapping of graphene and DNTT. Additionally, as shown in Fig. 5(g–i), higher hydrogen coverage would make the DOS of hydrogen shift to a high frequency, which also inhibits the direct energy transport from hydrogen to DNTT to some extent.

Similar to the effect of hydrogenation on the interfacial thermal conductance of a silicene/graphene bilayer investigated by Liu *et al.*,[39] this effect of hydrogenation on the TBR is further confirmed by alternately turning off the interaction of "C" or "H" with the atoms of DNTT (see Fig. S3 in the ESI†). We find out that when the interaction of "C" with DNTT is turned off, the TBR value becomes one order of magnitude larger. Besides, the contribution from "C" of hydrogenated graphene to interfacial thermal transport surpasses the direct effect from "H" of hydrogenated graphene. It is important to mention that although graphene hydrogenation reduces the thermal conductivity of graphene,[34,35,64] it can still enhance interfacial thermal transport of graphene and DNTT. This enhancement can be summarized into three major reasons: (a) higher phonon transmission capacity between graphene and DNTT; (b) improved energy conversion between in-plane and out-of-plane phonons in graphene; (c) direct interaction of hydrogen atoms with atoms in DNTT molecules.

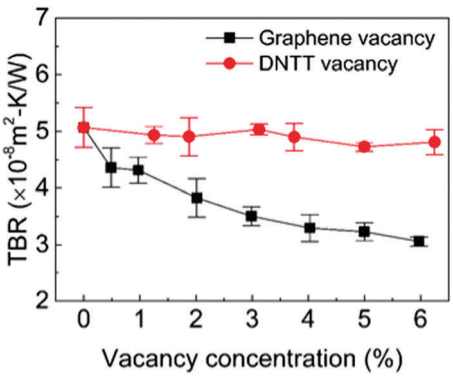

Fig. 6 TBR variation of graphene and DNTT at different graphene and DNTT vacancy concentrations.

3.3 Effects of vacancy defects

During the vapor phase deposition of graphene or organic semiconductors, vacancy defects due to the surface energy variations, impurities or roughness of the substrates are usually unavoidable. As these vacancies in the organic active layer will induce unpleasant effects on the device performance,[70–72] it is worth investigating their influence on the interfacial thermal transport. Firstly, we randomly delete some of the carbon atoms in graphene to create the single-vacancy defects in graphene while maintaining perfect DNTT. Then the DNTT molecules in the DNTT monolayer close to the interface are also randomly removed to create DNTT vacancies and graphene is kept pristine.

Fig. 6 exhibits the TBR variation with respect to the different graphene and DNTT vacancies. It can be noted that when graphene vacancies increase from 0% to 6%, TBR will reduce from $5.07 \pm 0.35 \times 10^{-8}$ m^2 K W^{-1} to $3.06 \pm 0.08 \times 10^{-8}$ m^2 K W^{-1}. This interesting observation suggests that although graphene vacancies would induce the phonon scattering in graphene sheets to block in-plane thermal transport of graphene,[29,30] the vacancies improve the out-of-plane interfacial thermal propagation. As shown in Fig. 7, similar to phonon DOS of hydrogenated graphene, graphene vacancies would broaden the phonon DOS of graphene and shift the G-band peak of graphene DOS, which enhances the overlapping areas of graphene and DNTT. In addition, graphene vacancies also increase the overlapping areas of the in-plane and out-of-plane DOS, which also benefits phonon transmission

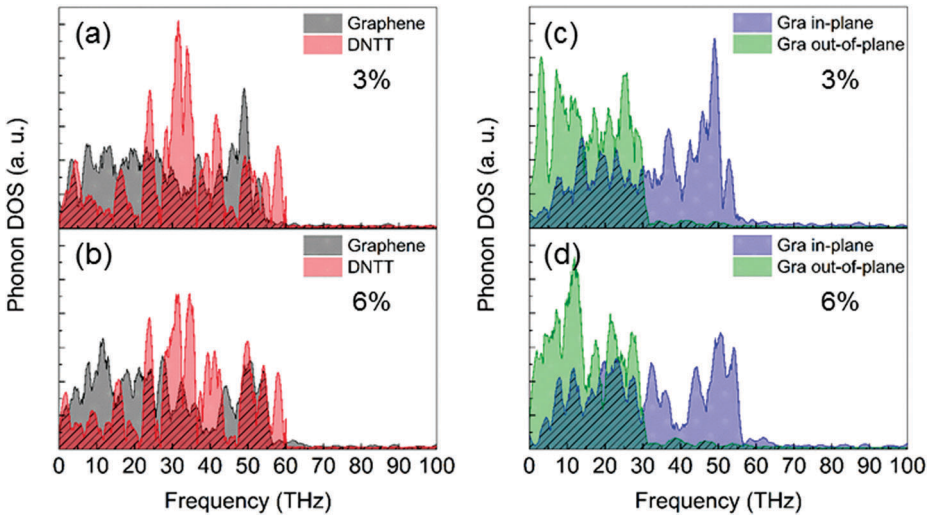

Fig. 7 (a and b) Phonon DOS of total graphene and DNTT at graphene vacancy concentration of 3% and 6%. (c and d) Phonon DOS of in-plane and out-of-plane graphene at graphene vacancy concentration of 3% and 6%. Slanted line areas denote overlap of phonon DOS. The phonon overlapping factors of graphene and DNTT are 0.633 and 0.643 at graphene vacancy concentration of 3% and 6%; and the phonon overlapping factors of in-plane and out-of-plane phonons in graphene are 0.489 and 0.501 at graphene vacancy concentration of 3% and 6%.

capacity across the interface between graphene and DNTT. In contrast, the TBR does not show an obvious dependence on DNTT vacancies as shown in Fig. 6. TBR maintains a constant level when the DNTT vacancy concentration changes from 0% to 6.25%. We also calculate the phonon DOS of total graphene, DNTT, in-plane graphene and out-of-plane graphene as shown in Fig. S4 in the ESI† and they show similar forms to those of the pristine graphene–DNTT structure without DNTT vacancies as shown Fig. 3. Therefore, although the thermal conductivity of organic semiconductors is susceptible to vacancies,[45,51] DNTT vacancies cannot affect the interfacial thermal transport between graphene and DNTT.

3.4 Effects of temperature and coupling strength

In the real application of graphene-based electronic devices, due to the complicated thermal environment, the devices would operate at a temperature range. Hence the temperature dependence of interfacial thermal transport of graphene and semiconductors is necessary to be studied to help to understand the thermal dissipating capability of devices. Additionally, the surface treatment in organic device fabrication is always used to modify the material interaction coupling at the heterojunction,[71,73–75] which immensely affects the electrical performance of devices. In this section, we also investigate the effect of coupling strength of graphene and DNTT by controlling the coupling strength factor, χ.

Firstly, we study the temperature dependence of TBR by tuning the equilibrium temperature in the *NVT* ensemble ranging from 100 K to 600 K. The coupling strength factor is still set to 1. As shown in Fig. 8, TBR would descend with an increase of temperature. When the temperature is 600 K, the TBR values of graphene–DNTT are $3.49 \pm 0.37 \times 10^{-8}$ m^2 K W^{-1}, which are 41.1% of the TBR values at 100 K ($8.50 \pm 0.20 \times 10^{-8}$ m^2 K W^{-1}). We attribute the reduction of TBR to the more phonon participation into interfacial thermal transport and stronger Umklapp phonon scattering. When temperature increases, more high-frequency phonons would be excited,[39,49] which enlarges the phonon transmission channel across graphene and DNTT. Furthermore, many theoretical and experimental studies have demonstrated that high temperature results in the enhancement of the Umklapp phonon scattering,[76] which plays a dominant role in interfacial thermal transport.[77,78] Strong Umklapp scattering would shorten the phonon mean free path and decompose the high-frequency phonons into more low-frequency phonons, which benefits the phonon coupling of graphene and DNTT as well as in-plane and out-of-plane phonon conversion of graphene. As a result, the temperature increase could make a significant contribution to the interfacial phonon propagation across graphene and DNTT.

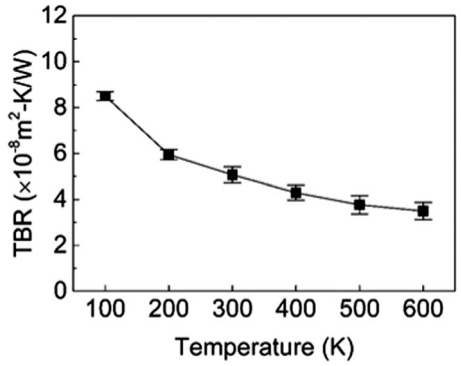

Fig. 8 TBR variation of graphene and DNTT at different temperatures from 100 K to 600 K.

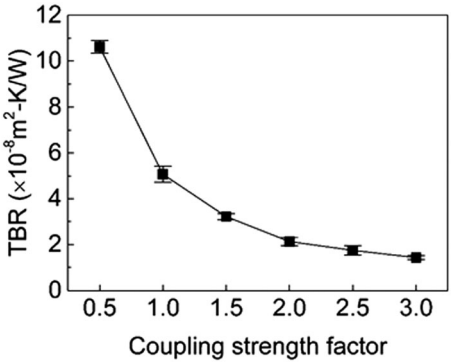

Fig. 9 TBR variation of graphene and DNTT at different coupling strength factors from 0.5 to 3.0.

The coupling strength is another key factor to affect the TBR of graphene and DNTT. In the simulations, we vary the coupling strength factor of van der Waals interaction of graphene and DNTT from 0.5 to 3.0. In Fig. 9, the TBR value of graphene and DNTT shows a monotonous downtrend. When the coupling strength increases from 0.5 to 3, the TBRs can drop around 86.5%. Because the interaction between graphene and the organic semiconductor mainly depends on the van der Waals forces of materials, the enhancement of the coupling strength factor will reinforce the interaction of graphene and DNTT, which further improves the energy transport capability across the interface. It is demonstrated that the surface treatment during the device fabrication not only affects the electrical properties, but also exerts the impact on the interfacial thermal transport.

4. Conclusions

The energy transport at the interfaces between graphene and the organic semiconductor plays a critical role in the performance and lifetime of the graphene-based organic electronic devices. In this study, we apply molecular dynamics simulations to study interfacial thermal transport across graphene and an organic semiconductor, dinaphtho[2,3-*b*:2′,3′-*f*]thieno-[3,2-*b*]thiophene (DNTT). The average TBR of graphene and DNTT is $4.88 \pm 0.12 \times 10^{-8}$ m^2 K W^{-1}, which does not show an obvious dependence on graphene and the DNTT size. We find that the hydrogenation of graphene is able to facilitate the heat transport across graphene and DNTT and TBRs can drop to around 8.4×10^{-9} m^2 K W^{-1} after graphene hydrogenation, which is attributed to enhanced phonon coupling of graphene and DNTT, better energy conversion of graphene in-plane and out-of-plane phonons and direct interaction of hydrogen with DNTT.

After adding the vacancy defects into DNTT and graphene, DNTT vacancy defects do not exert a significant effect on TBR while graphene vacancy defects can reduce from $5.07 \pm 0.35 \times 10^{-8}$ m^2 K W^{-1} to $3.06 \pm 0.08 \times 10^{-8}$ m^2 K W^{-1} as the graphene vacancy increases from 0% to 6%. Furthermore, we find that both temperature and coupling strength can reduce the TBR and benefit the interfacial thermal transport of graphene and DNTT. Our investigation about the interfacial thermal transport between graphene and organic semiconductors provides the fundamental knowledge to the design and development of graphene-based organic semiconductors.

Acknowledgements

We greatly appreciate the support from General Research Fund (GRF) under Grant No. HKU 710313E and 17200314, Collaborative Research Fund (CRF) under Grant No. C704514E, the National Natural Science Foundation of China (NSFC) and the Research Grants Council (RGC) of Hong Kong Joint Research Scheme under Grant No. HKU 715/14. This research is partially conducted by using the research computing facilities and advisory services offered by Information Technology Services at The University of Hong Kong.

References

1 Y. Zhang, Y.-W. Tan, H. L. Stormer and P. Kim, *Nature*, 2005, **438**, 201–204.
2 K. S. Novoselov, A. K. Geim, S. V. Morozov, D. Jiang, Y. Zhang, S. V. Dubonos, I. V. Grigorieva and A. A. Firsov, *Science*, 2004, **306**, 666–669.
3 J. Zhang, F. Xu, Y. Hong, Q. Xiong and J. Pan, *RSC Adv.*, 2015, **5**, 89415–89426.
4 L. Lindsay, D. A. Broido and N. Mingo, *Phys. Rev. B: Condens. Matter Mater. Phys.*, 2010, **82**, 115427.
5 J. Zhang, X. Wang and H. Xie, *Phys. Lett. A*, 2013, **377**, 721–726.
6 A. A. Balandin, S. Ghosh, W. Bao, I. Calizo, D. Teweldebrhan, F. Miao and C. N. Lau, *Nano Lett.*, 2008, **8**, 902–907.
7 Y.-M. Lin, K. A. Jenkins, A. Valdes-Garcia, J. P. Small, D. B. Farmer and P. Avouris, *Nano Lett.*, 2009, **9**, 422–426.
8 Y.-M. Lin, C. Dimitrakopoulos, K. A. Jenkins, D. B. Farmer, H.-Y. Chiu, A. Grill and P. Avouris, *Science*, 2010, **327**, 662.
9 X. Xu, L. F. C. Pereira, Y. Wang, J. Wu, K. Zhang, X. Zhao, S. Bae, C. Tinh Bui, R. Xie, J. T. L. Thong, B. H. Hong, K. P. Loh, D. Donadio, B. Li and B. Özyilmaz, *Nat. Commun.*, 2014, **5**, 3689.
10 B. D. Kong, S. Paul, M. B. Nardelli and K. W. Kim, *Phys. Rev. B: Condens. Matter Mater. Phys.*, 2009, **80**, 033406.
11 J. Cai, P. Ruffieux, R. Jaafar, M. Bieri, T. Braun, S. Blankenburg, M. Muoth, A. P. Seitsonen, M. Saleh, X. Feng, K. Mullen and R. Fasel, *Nature*, 2010, **466**, 470–473.
12 T. Ohta, A. Bostwick, T. Seyller, K. Horn and E. Rotenberg, *Science*, 2006, **313**, 951–954.
13 G. Fiori, S. Lebègue, A. Betti, P. Michetti, M. Klintenberg, O. Eriksson and G. Iannaccone, *Phys. Rev. B: Condens. Matter Mater. Phys.*, 2010, **82**, 153404.
14 A. K. Singh and B. I. Yakobson, *Nano Lett.*, 2009, **9**, 1540–1543.
15 J. Park, W. H. Lee, S. Huh, S. H. Sim, S. B. Kim, K. Cho, B. H. Hong and K. S. Kim, *J. Phys. Chem. Lett.*, 2011, **2**, 841–845.
16 Y. Wang, X. Chen, Y. Zhong, F. Zhu and K. P. Loh, *Appl. Phys. Lett.*, 2009, **95**, 063302.
17 W. Hong, Y. Xu, G. Lu, C. Li and G. Shi, *Electrochem. Commun.*, 2008, **10**, 1555–1558.
18 J. Huang, D. R. Hines, B. J. Jung, M. S. Bronsgeest, A. Tunnell, V. Ballarotto, H. E. Katz, M. S. Fuhrer, E. D. Williams and J. Cumings, *Org. Electron.*, 2011, **12**, 1471–1476.
19 S. Chung, J.-H. Lee, J. Jeong, J.-J. Kim and Y. Hong, *Appl. Phys. Lett.*, 2009, **94**, 253302.
20 C. Pannemann, T. Diekmann and U. Hilleringmann, *J. Mater. Res.*, 2004, **19**, 1999–2002.
21 E. Vitoratos, S. Sakkopoulos, E. Dalas, N. Paliatsas, D. Karageorgopoulos, F. Petraki, S. Kennou and S. A. Choulis, *Org. Electron.*, 2009, **10**, 61–66.
22 J. Zhang, Y. Wang and X. Wang, *Nanoscale*, 2013, **5**, 11598–11603.
23 Y. Hong, J. Zhang and X. C. Zeng, *Phys. Chem. Chem. Phys.*, 2016, **18**, 24164–24170.
24 M. Li, J. Zhang, X. Hu and Y. Yue, *Appl. Phys. A: Mater. Sci. Process.*, 2015, **119**, 415–424.
25 Y. Hong, L. Li, X. C. Zeng and J. Zhang, *Nanoscale*, 2015, **7**, 6286–6294.
26 Z. Chen, W. Jang, W. Bao, C. N. Lau and C. Dames, *Appl. Phys. Lett.*, 2009, **95**, 161910.
27 Y. Wang, A. K. Vallabhaneni, B. Qiu and X. Ruan, *Nanoscale Microscale Thermophys. Eng.*, 2014, **18**, 155–182.
28 Y. Wang, S. Chen and X. Ruan, *Appl. Phys. Lett.*, 2012, **100**, 163101.
29 H. Zhang, G. Lee and K. Cho, *Phys. Rev. B: Condens. Matter Mater. Phys.*, 2011, **84**, 115460.
30 F. Hao, D. Fang and Z. Xu, *Appl. Phys. Lett.*, 2011, **99**, 041901.
31 J.-W. Jiang, J. Lan, J.-S. Wang and B. Li, *J. Appl. Phys.*, 2010, **107**, 054314.
32 J. Hu, S. Schiffli, A. Vallabhaneni, X. Ruan and Y. P. Chen, *Appl. Phys. Lett.*, 2010, **97**, 133107.
33 Y. Tang, J. Li, X. Wu, Q. Liu, Y. Liu and P. Yang, *Appl. Surf. Sci.*, 2016, **362**, 86–92.
34 Q.-X. Pei, Z.-D. Sha and Y.-W. Zhang, *Carbon*, 2011, **49**, 4752–4759.
35 S.-K. Chien, Y.-T. Yang and C. O.-K. Chen, *Appl. Phys. Lett.*, 2011, **98**, 033107.
36 S.-K. Chien, Y.-T. Yang and C. O.-K. Chen, *Carbon*, 2012, **50**, 421–428.
37 S. Lin and M. J. Buehler, *Nanotechnology*, 2013, **24**, 165702.
38 B. Liu, J. A. Baimova, C. D. Reddy, S. V. Dmitriev, W. K. Law, X. Q. Feng and K. Zhou, *Carbon*, 2014, **79**, 236–244.
39 B. Liu, J. A. Baimova, C. D. Reddy, A. W.-K. Law, S. V. Dmitriev, H. Wu and K. Zhou, *ACS Appl. Mater. Interfaces*, 2014, **6**, 18180–18188.

40 Y. Hong, J. Zhang and X. C. Zeng, *Nanoscale*, 2016, **8**, 19211–19218.
41 Y. Hong, C. Zhu, M. Ju, J. Zhang and X. C. Zeng, *Phys. Chem. Chem. Phys.*, 2017, **19**, 6554–6562.
42 B. Liu, F. Meng, C. D. Reddy, J. A. Baimova, N. Srikanth, S. V. Dmitriev and K. Zhou, *RSC Adv.*, 2015, **5**, 29193–29200.
43 W. Xie, K. Willa, Y. Wu, R. Häusermann, K. Takimiya, B. Batlogg and C. D. Frisbie, *Adv. Mater.*, 2013, **25**, 3478–3484.
44 X. Wang, K. D. Parrish, J. A. Malen and P. K. L. Chan, *Sci. Rep.*, 2015, **5**, 16095.
45 X. Wang, J. Zhang, Y. Chen and P. K. L. Chan, *Nanoscale*, 2017, **9**, 2262–2271.
46 S. Plimpton, *J. Comput. Phys.*, 1995, **117**, 1–19.
47 W. B. Donald, A. S. Olga, A. H. Judith, J. S. Steven, N. Boris and B. S. Susan, *J. Phys.: Condens. Matter*, 2002, **14**, 783.
48 J. Zhang and X. Wang, *Nanoscale*, 2013, **5**, 734–743.
49 J. Zhang, Y. Hong and Y. Yue, *J. Appl. Phys.*, 2015, **117**, 134307.
50 J. Wang, R. M. Wolf, J. W. Caldwell, P. A. Kollman and D. A. Case, *J. Comput. Chem.*, 2004, **25**, 1157–1174.
51 D. Wang, L. Tang, M. Long and Z. Shuai, *J. Phys. Chem. C*, 2011, **115**, 5940–5946.
52 M. Yoneya, M. Kawasaki and M. Ando, *J. Mater. Chem.*, 2010, **20**, 10397–10402.
53 W. Shi, J. Chen, J. Xi, D. Wang and Z. Shuai, *Chem. Mater.*, 2014, **26**, 2669–2677.
54 A. K. Rappe, C. J. Casewit, K. S. Colwell, W. A. Goddard and W. M. Skiff, *J. Am. Chem. Soc.*, 1992, **114**, 10024–10035.
55 T. Yamamoto and K. Takimiya, *J. Am. Chem. Soc.*, 2007, **129**, 2224–2225.
56 J. Zhang, Y. Hong, Z. Tong, Z. Xiao, H. Bao and Y. Yue, *Phys. Chem. Chem. Phys.*, 2015, **17**, 23704–23710.
57 J. Zhang, Y. Hong, M. Liu, Y. Yue, Q. Xiong and G. Lorenzini, *Int. J. Heat Mass Transfer*, 2017, **104**, 871–877.
58 H. Zhong and J. R. Lukes, *Phys. Rev. B: Condens. Matter Mater. Phys.*, 2006, **74**, 125403.
59 D. L. Nika, A. S. Askerov and A. A. Balandin, *Nano Lett.*, 2012, **12**, 3238–3244.
60 T. Luo and J. R. Lloyd, *Adv. Funct. Mater.*, 2012, **22**, 2495–2502.
61 Y. Liu, C. Hu, J. Huang, B. G. Sumpter and R. Qiao, *J. Chem. Phys.*, 2015, **142**, 244703.
62 Y. Liu, J. Huang, B. Yang, B. G. Sumpter and R. Qiao, *Carbon*, 2014, **75**, 169–177.
63 Q. X. Pei, Y. W. Zhang and V. B. Shenoy, *Carbon*, 2010, **48**, 898–904.
64 B. Liu, C. D. Reddy, J. Jiang, J. A. Baimova, S. V. Dmitriev, A. A. Nazarov and K. Zhou, *Appl. Phys. Lett.*, 2012, **101**, 211909.
65 J. Zhou, Q. Wang, Q. Sun, X. S. Chen, Y. Kawazoe and P. Jena, *Nano Lett.*, 2009, **9**, 3867–3870.
66 R. R. Nair, W. Ren, R. Jalil, I. Riaz, V. G. Kravets, L. Britnell, P. Blake, F. Schedin, A. S. Mayorov, S. Yuan, M. I. Katsnelson, H.-M. Cheng, W. Strupinski, L. G. Bulusheva, A. V. Okotrub, I. V. Grigorieva, A. N. Grigorenko, K. S. Novoselov and A. K. Geim, *Small*, 2010, **6**, 2877–2884.
67 D. W. Boukhvalov, M. I. Katsnelson and A. I. Lichtenstein, *Phys. Rev. B: Condens. Matter Mater. Phys.*, 2008, **77**, 035427.
68 D. C. Elias, R. R. Nair, T. M. G. Mohiuddin, S. V. Morozov, P. Blake, M. P. Halsall, A. C. Ferrari, D. W. Boukhvalov, M. I. Katsnelson, A. K. Geim and K. S. Novoselov, *Science*, 2009, **323**, 610–613.
69 J. H. Seol, I. Jo, A. L. Moore, L. Lindsay, Z. H. Aitken, M. T. Pettes, X. Li, Z. Yao, R. Huang, D. Broido, N. Mingo, R. S. Ruoff and L. Shi, *Science*, 2010, **328**, 213–216.
70 A. Poschlad, V. Meded, R. Maul and W. Wenzel, *Nanoscale Res. Lett.*, 2012, **7**, 1–5.
71 R. Ruiz, D. Choudhary, B. Nickel, T. Toccoli, K.-C. Chang, A. C. Mayer, P. Clancy, J. M. Blakely, R. L. Headrick, S. Iannotta and G. G. Malliaras, *Chem. Mater.*, 2004, **16**, 4497–4508.
72 S. Seo, L. C. Grabow, M. Mavrikakis, R. J. Hamers, N. J. Thompson and P. G. Evans, *Appl. Phys. Lett.*, 2008, **92**, 153313.
73 B. Nickel, R. Barabash, R. Ruiz, N. Koch, A. Kahn, L. C. Feldman, R. F. Haglund and G. Scoles, *Phys. Rev. B: Condens. Matter Mater. Phys.*, 2004, **70**, 125401.
74 H. Chang, Y. Deng, Y. Geng, T. Wang and D. Yan, *Org. Electron.*, 2015, **22**, 86–91.
75 M.-C. Jung, M. R. Leyden, G. O. Nikiforov, M. V. Lee, H.-K. Lee, T. J. Shin, K. Takimiya and Y. Qi, *ACS Appl. Mater. Interfaces*, 2015, **7**, 1833–1840.
76 M. G. Holland, *Phys. Rev.*, 1963, **132**, 2461–2471.
77 P. E. Hopkins, P. M. Norris and R. J. Stevens, *J. Heat Transfer*, 2008, **130**, 022401.
78 P. E. Hopkins and P. M. Norris, *J. Heat Transfer*, 2009, **131**, 022402.